Multimodal Nonlinear Vibrational Hyperspectral Imaging

Jackson C. Wagner[1], Zishan Wu[1], Wei Xiong[1,2,3*]*

[1]Department of Chemistry and Biochemistry, UC San Diego, La Jolla, CA, 92093

[2]Materials Science and Engineering Program, UC San Diego, La Jolla, CA, 92093

[3]Department of Electrical and Computer Engineering, UC San Diego, La Jolla, CA, 92093

Email: jcwagner@ucsd.edu

ABSTRACT: Linescanning vibrational sum-frequency generation (VSFG) hyperspectral microscopy was developed into an inverted microscope design. The geometry enables seamless collection of brightfield, second-harmonic generation (SHG), and VSFG images of a given sample area. The new vertical configuration also enables future application to biologically relevant environments. The instrument is capable of simultaneously reporting on spatially resolved chemical and geometric specific sample characteristics. This capability is demonstrated with three samples: lyophilized collagen, a molecular self-assembly of sodium dodecyl sulfate and β-cyclodextrin (SDS@2β-CD), and a L-phenylalanyl-L-phenylalanine (FF) self-assembly. Hyperspectral analysis showed that the FF samples have anisotropic structural alignment, which is uniform along the long axis and structurally evolving along the short radial axis. Because all three samples represent protein and molecular hierarchically organized materials in the biomaterial and biomimetic fields, this work highlights the chemical-physical information VSFG microscopy can reveal to help in the bottom-up design and characterization of biomaterials.

Introduction

Organization of biomolecules into mesoscopic architectures is a ubiquitous process in natural and synthetic biomaterial formation.[1–6] Natural biomaterials are primarily comprised of organic subunits that assemble into higher-order hierarchical organizations. This process leverages the natural chemical composition and geometric configuration of molecular subunits to construct larger, functional architectures with function increased beyond the properties of the original molecular subunits.[7] For example, collagen is a biomaterial found in vertebrate animals that is categorized into 28 subtypes, each with unique chemical and physical properties that serve a specific biological function.[6,8,9] Collagen can take the form of a variety of tissues such as cartilage, bone, blood vessels as well as different types of connective tissues because of the different subtypes and its hierarchical organization.[10–12] The chemical and structural dependence is so strong that misalignment due to construction or composition defects leads to a change in its physical properties such as a reduction in its flexibility corresponding with an increase in stiffness.[13–15] Changes in the collagens physical and chemical properties has been shown to increase cancer proliferation as well.[16–18] Hierarchical organization has also been observed in biomimetics, a fields that seeks to synthesize biologically inspired structures.[19] Similarly, the ultimate function of the materials is correlated with the chemical composition and geometric of the fundamental subunits that comprise larger mesoscopic architectures.[20,21]

With structure and composition playing an important role in the properties of biomaterials, it is necessary to probe the chemical composition and higher-order hierarchical structures simultaneously. Specifically, understanding microscopic details and how they relate to mesoscopic structures of biomaterials [22] requires both molecular composition information from IR spectroscopy and spatial profiles afforded by microscopy. The mid-infrared (MIR) spectrum offers a wealth of chemical specific information through molecular vibrational modes.[23] Even better, FTIR microscopy (FTIRM) has shown the power of revealing spatially resolved, chemical specific details of biologically relevant samples [24]. However, based on a linear optical signal, FTIRM has limited sensitivity to structural organization and alignments. Also, since IR signals probe all IR active vibrational modes in the samples, the spectral signatures become complex and difficult to correlate spectral information to that of chemical organization.

On the other hand, structural imaging can be realized through second-order nonlinear optical signals such as second-harmonic generation (SHG) and vibrational sum-frequency generation (VSFG) spectroscopy. SHG and VSFG are only sensitive to environments that are noncentrosymmetric (e.g. lack inversion symmetry) and have been used to study biomaterials such as collagen and celliluse.[25–39] When using SHG and VSFG to study these tissues, its anisotropic chiral organization leads to tissue-only signals, ignoring the bulk surroundings.[32] While both are sensitive to structural arrangement, VSFG has the additional advantage of extracting chemical specific information because it measures molecular vibrational modes. [22,29,30,40–48] Broadband VSFG employs a resonant femtosecond IR pulse spatially and temporally overlapped with a nonresonant visible or NIR beam to coherently generate a signal at the sum of the energy of the two input beams. With the availability of tunable IR sources, in the form of optical parametric amplifiers (OPAs) and optical parametric oscillators (OPOs), VSFG can cover

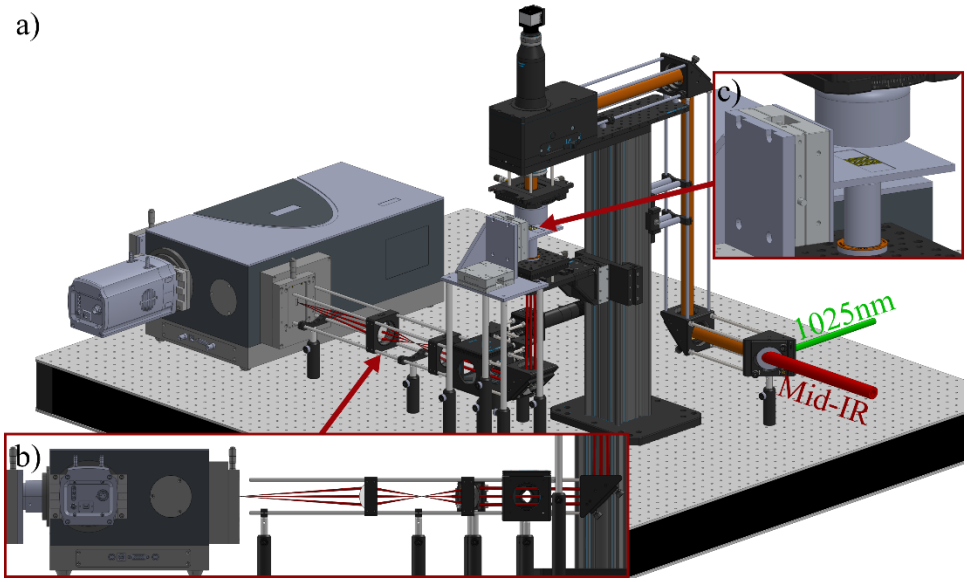

Figure 1. 3D model of inverted linescanning VSFG microscope. **a)** Linearly polarized 1μm and MIR beams are overlapped at a customized dichroic mirror. Beams are focused through the purely reflective condenser objective into a line with a resonant beam scanner. The generated VSFG signal is collected with an infinity corrected refractive based objective with an image being formed with a telescopic tube lens system on the entrance slit of the CCD/monochromator. **b)** Detailed view of variable tube lens set-up. The resultant line of images is shown in the red VSFG signal trace where the images is formed at the entrance slit of the monochromator. **c)** Detailed view of samples area where the reflective based Schwarzschild condenser at the top tightly achromatically focuses the light onto the sample area. Areas that have proper, symmetry and composition produce VSFG signals which are imaged with refractive a based imaging objective at the bottom in an inverted microscope geometry.

any VSFG active vibrational modes. The geometric details at molecular frame can then be extracted from VSFG images in the lab frame[49–51] by varying the polarization combination of the two input and one output beams, from which molecular orientation or intermolecular distances can be deduced.

Our group and others have developed the VSFG microscopy platform to accept biomimetic and biological materials.[22,29,30,40,41,43,44,46,47,52,53] Briefly, we have implemented a point-scanning VSFG microscope and used it to demonstrate superior phase stability for heterodyne detected VSFG images[41], and the importance of visualizing local ordering in an overall disordered system. We further used it to resolve hydration levels of self-assembled biomimetic sheets at the single domain level[29], and even conducted the first ultrafast vibrational dynamics of individual self-assembled sheets and reveal the heterogeneous hydration among sheets[22]. Recently, we further developed the point scanning geometry to a fast scanning VSFG microscope that can acquire data 10 times faster than the original point-scanning version[53]. This development reduced optomechanical and electronic instability in the system over the course of data collection. Although we were able to reduce collection times, the original fast scanning microscope was not integrated with other imaging modalities, such as brightfield or SHG microscopy, making comparison between images from different modalities difficult. Furthermore, the original fast-scanning setup adopted horizontal geometry which limited samples fixed to a substrate.

Building off our previous work[53], we incorporate and report here, an inverted multimodal microscope. The new microscope enabled seamless collection of VSFG, SHG, and brightfield microscopy images. Using this new setup, we collected VSFG spectra from 3 to 6 μm to explore resonant vibrational features that exist in samples, which allows the exploration of chemical specific geometric characteristics of the sample. Hyperspectral analysis of images at a spectral region of interest is performed to correlate spatial, chemical, and morphological details. This new setup is versatile and can be used on a variety of samples: SDS@2β-CD, lyophilized collagen, and L-phenylalanyl-L-phenylalanine (FF), as demonstrated below. Through in-depth hyperspectral analysis of the FF sample, we show that the FF sample has anisotropic structural arrangement which is homogeneous along the long axis and evolving along the radial axis. Spectral analysis also suggests that the sample is primarily composed of β-sheets across the entirety of the sample whereas towards the center helical formations exist. The range of samples provides evidence to the broad applicability for this microscope and potential impact to reveal chemical and structural information of biological and materials samples.

VSFG Microscope

The inverted hyperspectral VSFG microscope builds on previous designs of a VSFG imaging setup[53]. A SolidWorks sketch of the inverted hyperspectral VSFG microscope can be found in Figure 1. An optical parametric amplifier (Orpheus-HP, Light conversion) pumped by an Ytterbium doped seed laser (Carbide, Light Conversion) (230fs, 200μJ, 200kHz) generates the broadband mid-IR pulse centered at 3.5μm to study the -CH_x modes (~2900 cm^{-1}) or 6 μm for Amide bands (~1650 cm^{-1}). The mid-IR is colinearly overlapped with the narrowband upconversion beam (centered at 1025 nm) using a custom dichroic mirror. Both beams' polarizations are controlled with λ/2 waveplates and linear polarizers to guarantee pure polarization prior to the dichroic. The overlapped beams are dispersed into a line by a resonant scanner (Electrooptical Products Corp, 425Hz, 1° scan angle) and directed through the infinity corrected condenser objective (Pike Technologies Inc., 891-0001, 0.70NA)), a purely reflective optic which mitigates chromatic aberration from the large difference in frequency between the mid-IR (~3.5/6μm) and NIR (~1μm) pulses. The

beams are focused downwards through inverted microscope geometry onto a sample stage mounted to a 3-axis nano-positioner/encoder (MadCity Labs. MMP3) to generate the VSFG signal centered at ~800 nm. The VSFG signal is imaged by an infinity corrected refractive objective (Zeiss, 420150-9900-000) and the collimated signal is sent through a home built telescopic tube lens system composed of two f = 60 mm lenses. The VSFG signal is spectrally and spatially resolved simultaneously using a Chezny-Turner monochromator (Andor, Shamrock 500i) coupled to a CCD (Andor, Newton, DU920 Bx-DD) which collects spectrally resolved line sections of the image. To generate a full image, the 3-axis nano-position is rastered in 1-axis.

Results and Discussion

Multi-modal imaging

The vertical VSFG microscope enables multi-modal imaging, including optical, SHG and VSFG images. Brightfield images were collected using a white light illumination source. This enabled the exploration and inspection of interesting sample locations. This important development reduced the time it took to locate samples on the glass coverslips. SHG images can also be collected by blocking the MIR beam and exclusively imaging the signal at the second harmonic of the up-conversion beam (~515nm). Lastly, VSFG spectra were collected for the amide (1650cm^{-1}) and -CH (2900cm^{-1}) regions to gain knowledge of the chemical compositions and environment experienced by the materials.

The images of SDS@2β-CD, lyophilized collagen, and FF are shown in Figure 2, where a-c represents the three samples, and i – iv representing the optical, SHG, CH_x and Amide VSFG images, respectively. The SHG and VSFG intensity images agreed with profiles of brightfield images nicely when overlaid. However, the SHG and VSFG spectra also show differences from the optical images, depending on samples. For both SDS@2β-CD and FF samples, the nonlinear optical images are homogeneous across the samples, indicating homogeneous alignments and orientations across the samples. In contrast, the signal intensity of SHG and VSFG images of the lyophilized collagen samples were very heterogeneous. Only a sub-ensemble of region has high intensity in both SHG and VSFG images. These bright regions could reflect areas that are ordered, or the molecular modes are close to parallel to the laser polarizations.

A quick, qualitative comparison between the CH_x and amide spectral regions of FF and lyophilized collagen, shown in Figure 2, reveals the local structural ordering of a particular spectral region. For example, if both functional groups are homogeneously ordered across the sample space, we would expect the images at either spectral region to have similar intensity maps. This is true for the FF sample (Figure 2c_{iii}-c_{iv}) which exhibits homogeneity across spectral regions. Alternatively, if functional groups have dissimilar ordering in the local organization, VSFG hyperspectral imaging would reveal this, where the two functional groups would have different intensity maps. This is the case for lyophilized collagen in the CH_x and amide region intensity maps (Figure 2b_{iii} and b_{iv}) which show differences in the relative spectral intensities between the two spectral regions.

Hyperspectral analysis

The comparison between SHG and VSFG intensity mapped images only reveal part of the power of the inverted line scanning VSFG microscope. Each VSFG image indeed contains a spectrum that encodes a material's chemical structural information. Thus, the VSFG image are hyperspectral data cubes with two spatial dimensions, which form an x-y sample space, and one spectral dimension, which contains rich information of the sample's microscopic and mesoscopic structures. We use the MATLAB hyperspectral processing toolbox to analyze the data. Each pixel of the hyperspectral data cube is then assigned to one identified unique spectra to generate an image based on spectral similarity. Analyzing images with this approach enables direct

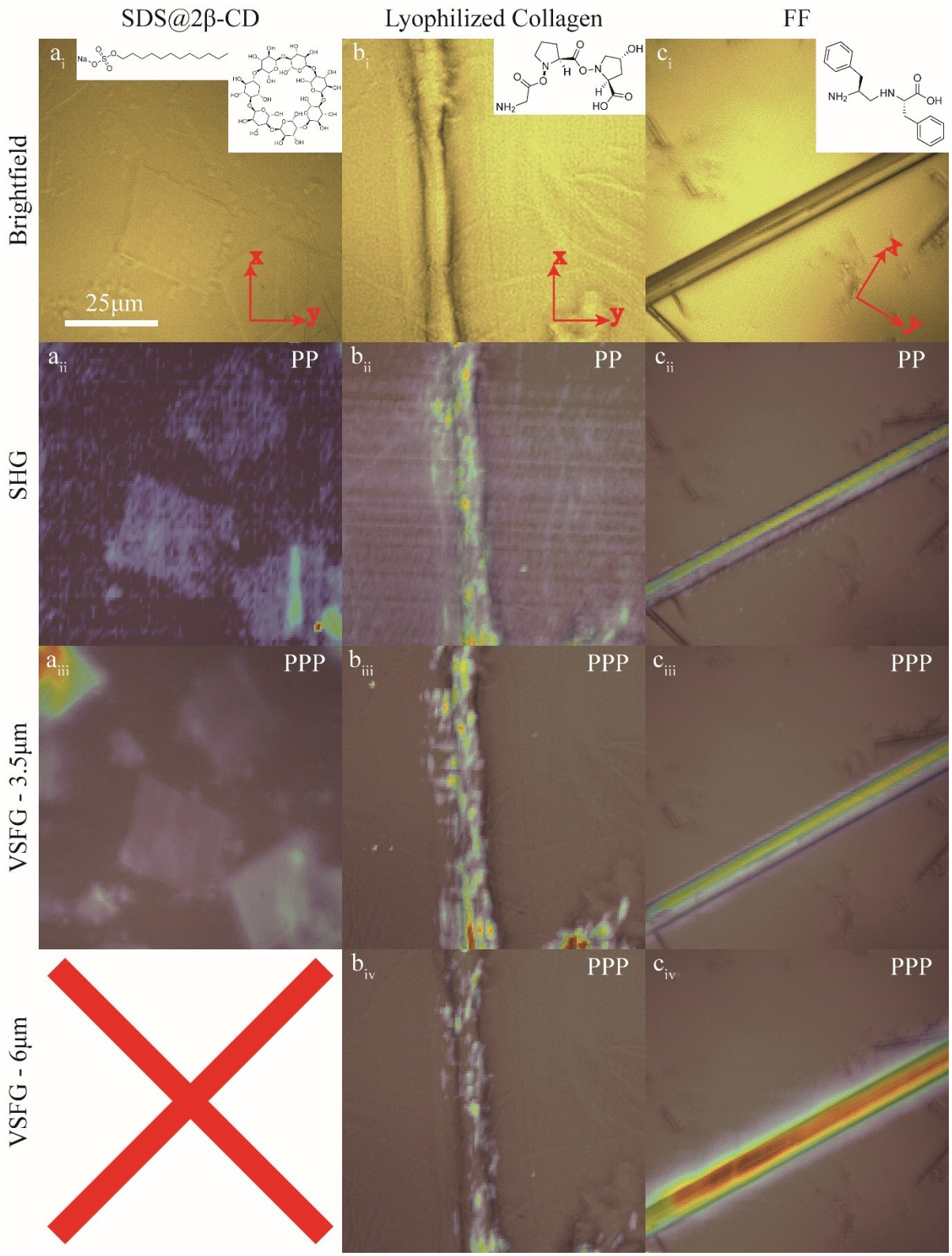

Figure 2. Multi-modal images of three different samples. **a_i-a_{iii})** SDS@2β-CD brightfield, SHG (PP polarization) and, VSFG (PPP polarization) of 3.5μm region images respectively. Nonlinear images are overlaid with brightfield images. Chemical structures of SDS and 2β-CD are shown in the inset of **a_i**. **b_i-b_{iv})** Lyophilized collagen brightfield, SHG (PP polarization), VSFG (PPP polarization) of 3.5μm and 6μm regions respectively. Chemical structure of the primary protein trimer residue of collagen, composed of glycine, proline and hydroxyproline is shown in the inset of **b_i**. **c_i-c_{iv})** FF brightfield, SHG (PP polarization), and VSFG (PPP polarization) of 3.5μm and 6μm regions respectively. Chemical structure for the FF molecular subunits is shown in the inset of **c_i**. All 6μm images are taken under a purged nitrogen instrument environment to remove attenuation from ambient air moisture.

correlation between spectral signatures and their spatial location in the sample.

To show the proof-of-principle, we focus on FF sample. SDS@2β-CD has been analyzed by us previously[22,29,40,41,53] and the collagen hyperspectra are complicated which we will discuss in future publications. The spectral similarity images of FF for both the -CH and amide spectral regions are summarized in Figure 3. In both regions,

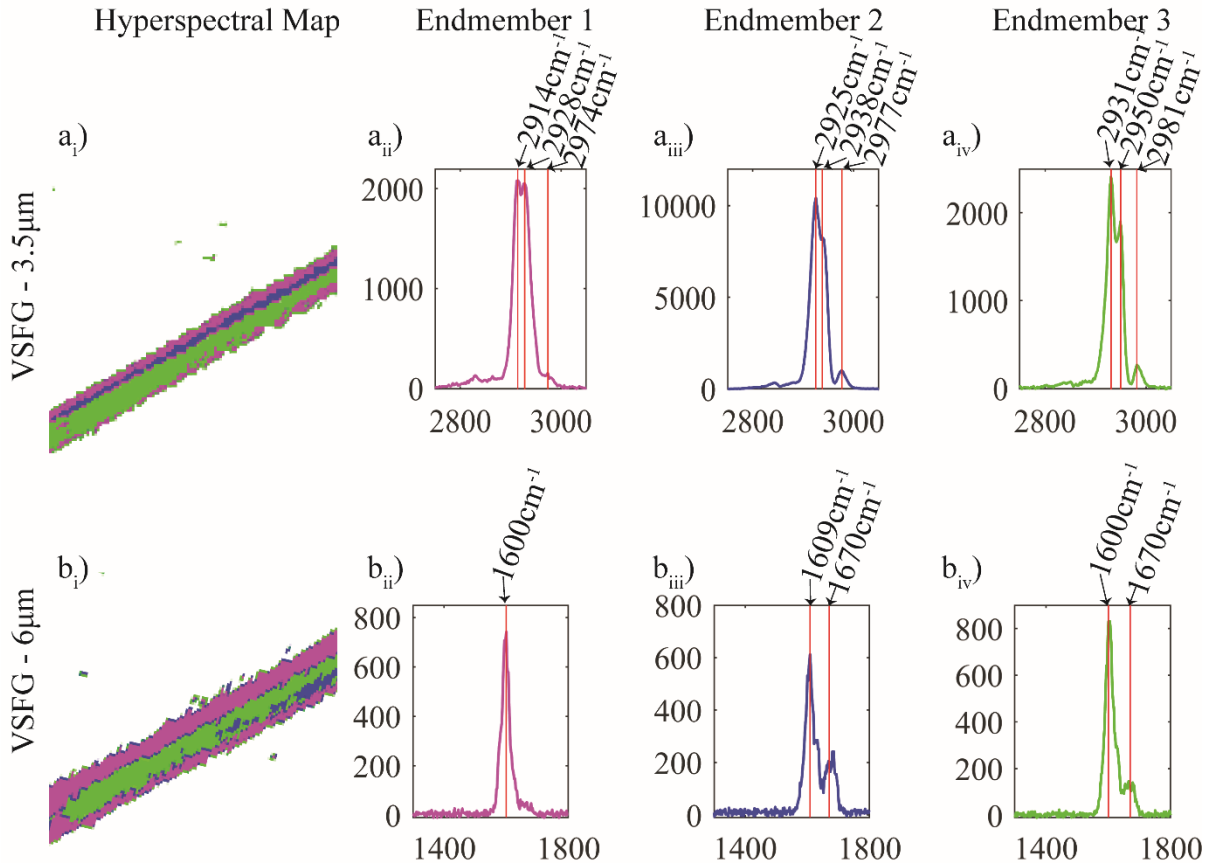

Figure 3. Hyperspectral analysis of VSFG images. **a_i-a_{iv})** Hyperspectral image of FF with 3.5μm MIR, endmembers 1, 2 and, 3 respectively. Each endmember corresponds to unique spectra identified within the hyperspectral data cube at that frequency. **b_i-b_{iv})** Hyperspectral image of FF with 6μm MIR, endmembers 1, 2 and, 3 respectively. Each endmember corresponds to unique spectra identified within the hyperspectral data cube at that frequency. Comparing the three unique peaks and their spatial locations in both 3.5μm and 6μm, we observe similarities in their location between the two spectral regions.

three unique spectra were identified. The corresponding pixels of the spectra were then color coded in the images. The three unique spectra identified in the -CH region image (Figure 3a_{ii}-a_{iv}) have different intensity and spectral shape. In all three identified unique spectra, there are three primary peaks in the -CH region, 2915cm^{-1}, 2930cm^{-1}, 2970cm^{-1}, corresponding to antisymmetric stretch of -CH_2, fermi resonance of CH_3, and potentially the C_α-H modes.[54] However, the main difference between the three identified unique spectra can be found when comparing the magenta and green labeled areas where the CH_2 antisymmetric stretch and CH_3 fermi resonance blue shift by about 10-20cm^{-1}. The peak shifts were further visualized by checking the VSFG spectra across the radial direction of the FF needles using the MATLAB hyperspectral imaging toolbox (see web-enhanced object video 1). The origin of the blue shift could be due to slight conformational differences that exist on the micron scale.[55,56] However, the exact conformational changes remain unclear. It is noticeable that the spectra only shift along the radial axis, while are uniform along the axial axis, which indicates an anisotropic structural arrangement: there are structural evolutions along the radial axis, and the structures are homogeneous along the long axis.

To further gain insights to the structural anisotropy, we analyzed the Amide region. We also identified three unique spectra (Figure 3b_{ii}-b_{iv}). It is noticeable that spectral distribution map (Figure 3b_i) also shows similar features as the -CH region: uniform along axial axis and evolving along radial directions. Thus, it further suggests that well-ordered self-assembled structures were formed and propagate along the axial directions.

The spectral features of the identified unique spectra, however, have similar spectral shape but different peak ratios between the higher and lower frequency features. (See Figure 3b_{ii}-b_{iv} and web-enhanced object video 1). The primary spectral features in the Amide region which exists across all three spectra at 1600cm^{-1} corresponds to β-sheet secondary structure. The 1670cm^{-1} only exists in endmember 1 and 3 spectra and could correspond to a 3_{10}-helix.[57–59] This peak assignment indicates that the FF micro needles are primarily in β-sheet formations on the extremes of the needle. Moving towards the center, the growth of the higher frequency feature could suggest helical structures also exist in this region.

Full spectral analysis

For each spatial pixels, we can also scan the OPA output to collect VSFG spectra from 3 to 6 μm. Collagen and FF samples, comprised almost exclusively of peptides, showed rich features in hydrocarbon (2800cm^{-1}-3100cm^{-1}), water (3000cm^{-1}-3500cm^{-1}) and amino (Amide A 3000cm^{-1}-3500cm^{-1}, Amide I, II, and III 1200cm^{-1}-1800cm^{-1}) groups, under PPP polarization (Figure 4). However, they showed very different lineshapes. The FF spectral features were sharp, while the collagen spectra were broad. The lineshape difference are most likely due to inhomogeneous broadening, suggesting them having different heterogeneity even within 1 micron region (the spatial resolution of the setup). This result agrees with the morphology of samples. FF forms microcrystalline, and therefore each unit cell experiences similar chemical environments, while the lyophilized collagens are soft tissues and thereby form very inhomogeneous chemical environment. However, it is not completely disordered as that would lead to null signal in VSFG.

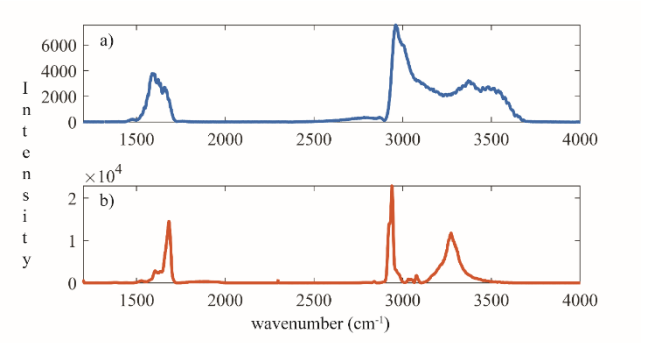

Figure 4. Comparison of full VSFG spectra of collagen and FF samples. **a)** Spectral scan of PPP configuration of lyophilized collagen. Distinct features are clearly shown in both the 2800cm^{-1}-3700cm^{-1} and 1500cm^{-1}-1700cm^{-1} regions. **b)** FF spectral scan under PPP polarization control for the same regions. Both spectra are collected in a nitrogen purged instrument atmosphere to remove spectral attenuation from ambient water absorption.

Conclusions and Outlook

Building off our previous VSFG microscope designs, SHG and brightfield imaging modalities were added to further improve VSFG microscopy's applicability, specifically to biological and biomimetic materials. The demonstration of the technique on three samples, SDS@2β-CD, lyophilized collagen, and diphenylalanine aggregates, highlight VSFG microscopy's capabilities to report spatially resolved, chemical specific information for all three samples.

When different spectra across the thickness of an FF microneedle were compared, nuanced differences in peak position, primarily in the 3.5μm region, were observed. In addition, the secondary structures of FF were elucidated through analysis of Amide-I region spectra and found to be primarily in a β-sheet configuration. Similar analyses of additional materials could reveal nuanced spatial heterogeneity of vibrational spectra which could further inform the biology, chemistry, and materials science fields, among others, of chemical environments and structural organization of materials. We note that the current system would benefit from an increase in resolution through super resolution techniques which would decrease the size of architectures that can be imaged with this microscope.

ASSOCIATED CONTENT

The Supporting Information is available free of charge via the Internet at http://pubs.acs.org.

AUTHOR INFORMATION

Corresponding Authors

Jackson Wagner - *Department of Chemistry and Biochemistry, University of California San Diego, La Jolla, California 92093*

Wei Xiong - *Department of Chemistry and Biochemistry, University of California San Diego, La Jolla, California 92093, United States*; *Materials Science and Engineering Program, University of California San Diego, La Jolla, California 92093, United States*; *Department of Electrical and Computer Engineering, University of California San Diego, La Jolla, California 92093, United States*.

Author Contributions

The manuscript was written through contributions of all authors.

Funding Sources

W.X. thank the development of instrument under NSF Major Research Instrumentation Grant CHE1828666. J.C.W. and Z. W. were supported by National Institutes of Health, National Institute of General Medical Sciences, Grant 1R35GM138092-01.

ACKNOWLEDGMENT

The authors would like to acknowledge Tianyi Shen, who synthesized the FF microneedles.

References

(1) Libonati, F.; Buehler, M. J. Advanced Structural Materials by Bioinspiration. *Adv. Eng. Mater.* **2017**, *19* (5), 1600787. https://doi.org/10.1002/adem.201600787.

(2) Yin, B. B.; Sun, W. K.; Zhang, X. Y.; Liew, K. M. Deciphering Structural Biological Materials: Viewing from the Mechanics Perspective and Their Prospects. *Compos. Part B Eng.* **2022**, *245*, 110213. https://doi.org/10.1016/j.compositesb.2022.110213.

(3) Egan, P.; Sinko, R.; LeDuc, P. R.; Keten, S. The Role of Mechanics in Biological and Bio-Inspired Systems. *Nat. Commun.* **2015**, *6* (1), 7418. https://doi.org/10.1038/ncomms8418.

(4) Hendrikse, S. I. S.; Contreras-Montoya, R.; Ellis, A. V.; Thordarson, P.; Steed, J. W. Biofunctionality with a Twist: The Importance of Molecular Organisation, Handedness and Configuration in Synthetic Biomaterial Design. *Chem. Soc. Rev.* **2022**, *51* (1), 28–42. https://doi.org/10.1039/D1CS00896J.

(5) Firipis, K.; Nisbet, D. R.; Franks, S. J.; Kapsa, R. M. I.; Pirogova, E.; Williams, R. J.; Quigley, A. Enhancing Peptide Biomaterials for Biofabrication. *Polymers (Basel).* **2021**, *13* (16), 2590. https://doi.org/10.3390/polym13162590.

(6) Amirrah, I. N.; Lokanathan, Y.; Zulkiflee, I.; Wee, M. F. M. R.; Motta, A.; Fauzi, M. B. A Comprehensive Review on Collagen Type I Development of Biomaterials for Tissue Engineering: From Biosynthesis to Bioscaffold. *Biomedicines* **2022**, *10* (9), 2307.

https://doi.org/10.3390/biomedicines10092307.

(7) Yuan, C.; Ji, W.; Xing, R.; Li, J.; Gazit, E.; Yan, X. Hierarchically Oriented Organization in Supramolecular Peptide Crystals. *Nat. Rev. Chem.* **2019**, *3* (10), 567–588. https://doi.org/10.1038/s41570-019-0129-8.

(8) Sherman, V. R.; Yang, W.; Meyers, M. A. The Materials Science of Collagen. *J. Mech. Behav. Biomed. Mater.* **2015**, *52*, 22–50. https://doi.org/10.1016/j.jmbbm.2015.05.023.

(9) Ricard-Blum, S. The Collagen Family. *Cold Spring Harb. Perspect. Biol.* **2011**, *3* (1), a004978–a004978. https://doi.org/10.1101/cshperspect.a004978.

(10) Rhodes, J. M.; Simons, M. The Extracellular Matrix and Blood Vessel Formation: Not Just a Scaffold. *J. Cell. Mol. Med.* **2007**, *11* (2), 176–205. https://doi.org/10.1111/j.1582-4934.2007.00031.x.

(11) Nogueira, L. F. B.; Maniglia, B. C.; Buchet, R.; Millán, J. L.; Ciancaglini, P.; Bottini, M.; Ramos, A. P. Three-dimensional Cell-laden Collagen Scaffolds: From Biochemistry to Bone Bioengineering. *J. Biomed. Mater. Res. Part B Appl. Biomater.* **2022**, *110* (4), 967–983. https://doi.org/10.1002/jbm.b.34967.

(12) Rezvani Ghomi, E.; Nourbakhsh, N.; Akbari Kenari, M.; Zare, M.; Ramakrishna, S. Collagen-based Biomaterials for Biomedical Applications. *J. Biomed. Mater. Res. Part B Appl. Biomater.* **2021**, *109* (12), 1986–1999. https://doi.org/10.1002/jbm.b.34881.

(13) Goldberga, I.; Li, R.; Duer, M. J. Collagen Structure–Function Relationships from Solid-State NMR Spectroscopy. *Acc. Chem. Res.* **2018**, *51* (7), 1621–1629. https://doi.org/10.1021/acs.accounts.8b00092.

(14) Zhu, S.; Yuan, Q.; Yin, T.; You, J.; Gu, Z.; Xiong, S.; Hu, Y. Self-Assembly of Collagen-Based Biomaterials: Preparation, Characterizations and Biomedical Applications. *J. Mater. Chem. B* **2018**, *6* (18), 2650–2676. https://doi.org/10.1039/C7TB02999C.

(15) Marro, M.; Kossar, A. P.; Xue, Y.; Frasca, A.; Levy, R. J.; Ferrari, G. Noncalcific Mechanisms of Bioprosthetic Structural Valve Degeneration. *J. Am. Heart Assoc.* **2021**, *10* (3). https://doi.org/10.1161/JAHA.120.018921.

(16) Xu, S.; Xu, H.; Wang, W.; Li, S.; Li, H.; Li, T.; Zhang, W.; Yu, X.; Liu, L. The Role of Collagen in Cancer: From Bench to Bedside. *J. Transl. Med.* **2019**, *17* (1), 309. https://doi.org/10.1186/s12967-019-2058-1.

(17) Velez, D. O.; Ranamukhaarachchi, S. K.; Kumar, A.; Modi, R. N.; Lim, E. W.; Engler, A. J.; Metallo, C. M.; Fraley, S. I. 3D Collagen Architecture Regulates Cell Adhesion through Degradability, Thereby Controlling Metabolic and Oxidative Stress. *Integr. Biol.* **2019**, *11* (5), 221–234. https://doi.org/10.1093/intbio/zyz019.

(18) Ranamukhaarachchi, S. K.; Modi, R. N.; Han, A.; Velez, D. O.; Kumar, A.; Engler, A. J.; Fraley, S. I. Macromolecular Crowding Tunes 3D Collagen Architecture and Cell Morphogenesis. *Biomater. Sci.* **2019**, *7* (2), 618–633. https://doi.org/10.1039/C8BM01188E.

(19) Lizundia, E.; Nguyen, T.-D.; Winnick, R. J.; MacLachlan, M. J. Biomimetic Photonic Materials Derived from Chitin and Chitosan. *J. Mater. Chem. C* **2021**, *9* (3), 796–817. https://doi.org/10.1039/D0TC05381C.

(20) Makam, P.; Gazit, E. Minimalistic Peptide Supramolecular Co-Assembly: Expanding the Conformational Space for Nanotechnology. *Chem. Soc. Rev.* **2018**, *47* (10), 3406–3420. https://doi.org/10.1039/C7CS00827A.

(21) Yang, S.; Yan, Y.; Huang, J.; Petukhov, A. V.; Kroon-Batenburg, L. M. J.; Drechsler, M.; Zhou, C.; Tu, M.; Granick, S.; Jiang, L. Giant Capsids from Lattice Self-Assembly of Cyclodextrin Complexes. *Nat. Commun.* **2017**, *8* (May), 1–7. https://doi.org/10.1038/ncomms15856.

(22) Wang, H.; Wagner, J. C.; Chen, W.; Wang, C.; Xiong, W. Spatially Dependent H-Bond Dynamics at Interfaces of Water/Biomimetic Self-Assembled Lattice Materials. *Proc. Natl. Acad. Sci.* **2020**, *117* (38), 23385–23392. https://doi.org/10.1073/pnas.2001861117.

(23) Pallua, J. D.; Brunner, A.; Zelger, B.; Stalder, R.; Unterberger, S. H.; Schirmer, M.; Tappert, M. C. Clinical Infrared Microscopic Imaging: An Overview. *Pathol. - Res. Pract.* **2018**, *214* (10), 1532–1538. https://doi.org/10.1016/j.prp.2018.08.026.

(24) Lazaro-Pacheco, D.; Shaaban, A.; Baldwin, G.; Titiloye, N. A.; Rehman, S.; Rehman, I. ur. Deciphering the Structural and Chemical Composition of Breast Cancer Using FTIR Spectroscopy. *Appl. Spectrosc. Rev.* **2022**, *57* (3), 234–248. https://doi.org/10.1080/05704928.2020.1843471.

(25) James, D. S.; Campagnola, P. J. Recent Advancements in Optical Harmonic Generation Microscopy: Applications and Perspectives. *BME Front.* **2021**, *2021*, 1–24. https://doi.org/10.34133/2021/3973857.

(26) Li, R.; Wang, X.; Zhou, Y.; Zong, H.; Chen, M.; Sun, M. Advances in Nonlinear Optical Microscopy for Biophotonics. *J. Nanophotonics* **2018**, *12* (03), 1. https://doi.org/10.1117/1.JNP.12.033007.

(27) Inoue, K.; Ahmed, M.; Nihonyanagi, S.; Tahara, T. Reorientation-Induced Relaxation of Free OH at the Air/Water Interface Revealed by Ultrafast Heterodyne-Detected Nonlinear Spectroscopy. *Nat. Commun.* **2020**, *11* (1), 5344. https://doi.org/10.1038/s41467-020-19143-8.

(28) Ishiyama, T.; Kitanaka, K. Asymmetric Hydrogen-Bonding Structure at a Water/Ice Interface. *J. Phys. Chem. C* **2020**, *124* (42), 23287–23294. https://doi.org/10.1021/acs.jpcc.0c08173.

(29) Wang, H.; Chen, W.; Wagner, J. C.; Xiong, W. Local Ordering of Lattice Self-Assembled SDS@2β-CD Materials and Adsorbed Water Revealed by Vibrational Sum Frequency Generation Microscope. *J. Phys. Chem. B* **2019**, *123* (29), 6212–6221. https://doi.org/10.1021/acs.jpcb.9b04928.

(30) Chung, C.-Y.; Potma, E. O. Biomolecular Imaging with Coherent Nonlinear Vibrational Microscopy. *Annu. Rev. Phys. Chem.* **2013**, *64* (1), 77–99. https://doi.org/10.1146/annurev-physchem-040412-110103.

(31) Makarem, M.; Nishiyama, Y.; Xin, X.; Durachko, D. M.; Gu, Y.; Cosgrove, D. J.; Kim, S. H. Distinguishing Mesoscale Polar Order (Unidirectional vs Bidirectional) of Cellulose Microfibrils in Plant Cell

Walls Using Sum Frequency Generation Spectroscopy. *J. Phys. Chem. B* **2020**, *124* (37), 8071–8081. https://doi.org/10.1021/acs.jpcb.0c07076.

(32) Dudenkova, V. V.; Shirmanova, M. V.; Lukina, M. M.; Feldshtein, F. I.; Virkin, A.; Zagainova, E. V. Examination of Collagen Structure and State by the Second Harmonic Generation Microscopy. *Biochem.* **2019**, *84* (S1), 89–107. https://doi.org/10.1134/S0006297919140062.

(33) Kim, K.; Choi, S.; Zhang, Z.; Bai, L.; Chung, S.; Jang, J. Molecular Features of Hydration Layers: Insights from Simulation, Microscopy, and Spectroscopy. *J. Phys. Chem. C* **2022**, *126* (21), 8967–8977. https://doi.org/10.1021/acs.jpcc.2c01313.

(34) Xiang, B.; Li, Y.; Pham, C. H.; Paesani, F.; Xiong, W. Ultrafast Direct Electron Transfer at Organic Semiconductor and Metal Interfaces. *Sci. Adv.* **2017**, *3* (11). https://doi.org/10.1126/sciadv.1701508.

(35) Li, Y.; Shrestha, M.; Luo, M.; Sit, I.; Song, M.; Grassian, V. H.; Xiong, W. Salting Up of Proteins at the Air/Water Interface. *Langmuir* **2019**, *35* (43), 13815–13820. https://doi.org/10.1021/acs.langmuir.9b01901.

(36) Wang, C.; Li, Y.; Xiong, W. Extracting Molecular Responses from Ultrafast Charge Dynamics at Material Interfaces. *J. Mater. Chem. C* **2020**, *8* (35), 12062–12067. https://doi.org/10.1039/D0TC01819H.

(37) Li, Y.; Wang, J.; Xiong, W. Probing Electronic Structures of Organic Semiconductors at Buried Interfaces by Electronic Sum Frequency Generation Spectroscopy. *J. Phys. Chem. C* **2015**, *119* (50), 28083–28089. https://doi.org/10.1021/acs.jpcc.5b10725.

(38) Saha, S.; Roy, S.; Mathi, P.; Mondal, J. A. Polyatomic Iodine Species at the Air–Water Interface and Its Relevance to Atmospheric Iodine Chemistry: An HD-VSFG and Raman-MCR Study. *J. Phys. Chem. A* **2019**, *123* (13), 2924–2934. https://doi.org/10.1021/acs.jpca.9b00828.

(39) Okuno, M.; Yamada, S.; Ohto, T.; Tada, H.; Nakanishi, W.; Ariga, K.; Ishibashi, T. Hydrogen Bonds and Molecular Orientations of Supramolecular Structure between Barbituric Acid and Melamine Derivative at the Air/Water Interface Revealed by Heterodyne-Detected Vibrational Sum Frequency Generation Spectroscopy. *J. Phys. Chem. Lett.* **2020**, *11* (7), 2422–2429. https://doi.org/10.1021/acs.jpclett.0c00329.

(40) Wang, H.; Xiong, W. Vibrational Sum-Frequency Generation Hyperspectral Microscopy for Molecular Self-Assembled Systems. *Annu. Rev. Phys. Chem.* **2021**, *72* (1), 279–306. https://doi.org/10.1146/annurev-physchem-090519-050510.

(41) Wang, H.; Gao, T.; Xiong, W. Self-Phase-Stabilized Heterodyne Vibrational Sum Frequency Generation Microscopy. *ACS Photonics* **2017**, *4* (7), 1839–1845. https://doi.org/10.1021/acsphotonics.7b00411.

(42) Han, Y.; Raghunathan, V.; Feng, R. R.; Maekawa, H.; Chung, C.-Y. Y.; Feng, Y.; Potma, E. O.; Ge, N.-H. H. Mapping Molecular Orientation with Phase Sensitive Vibrationally Resonant Sum-Frequency Generation Microscopy. *J. Phys. Chem. B* **2013**, *117* (20), 6149–6156. https://doi.org/10.1021/jp4022147.

(43) Potma, E. O. Advances in Vibrationally Resonant Sum-Frequency Generation Microscopy. In *Optics in the Life Sciences Congress*; OSA: Washington, D.C., 2017; p NM4C.2. https://doi.org/10.1364/NTM.2017.NM4C.2.

(44) Han, Y.; Hsu, J.; Ge, N.-H.; Potma, E. O. Polarization-Sensitive Sum-Frequency Generation Microscopy of Collagen Fibers. *J. Phys. Chem. B* **2015**, *119* (8), 3356–3365. https://doi.org/10.1021/jp511058b.

(45) Raghunathan, V.; Han, Y.; Korth, O.; Ge, N.-H.; Potma, E. O. Rapid Vibrational Imaging with Sum Frequency Generation Microscopy. *Opt. Lett.* **2011**, *36* (19), 3891. https://doi.org/10.1364/OL.36.003891.

(46) Hanninen, A.; Shu, M. W.; Potma, E. O. Hyperspectral Imaging with Laser-Scanning Sum-Frequency Generation Microscopy. *Biomed. Opt. Express* **2017**, *8* (9), 4230. https://doi.org/10.1364/BOE.8.004230.

(47) Hsu, J.; Haninnen, A.; Ge, N.-H.; Potma, E. O. Molecular Imaging with Sum-Frequency Generation Microscopy. In *Optics in the Life Sciences*; OSA: Washington, D.C., 2015; p NT4C.4. https://doi.org/10.1364/NTM.2015.NT4C.4.

(48) Lee, C. M.; Kafle, K.; Huang, S.; Kim, S. H. Multimodal Broadband Vibrational Sum Frequency Generation (MM-BB-V-SFG) Spectrometer and Microscope. *J. Phys. Chem. B* **2016**, *120* (1), 102–116. https://doi.org/10.1021/acs.jpcb.5b10290.

(49) Wang *, H.-F.; Gan † ‡, W.; Lu † ‡ §, R.; Rao † ‡ ¶, Y.; Wu †, B.-H. Quantitative Spectral and Orientational Analysis in Surface Sum Frequency Generation Vibrational Spectroscopy (SFG-VS). *Int. Rev. Phys. Chem.* **2005**, *24* (2), 191–256. https://doi.org/10.1080/01442350500225894.

(50) Wang, H.-F.; Velarde, L.; Gan, W.; Fu, L. Quantitative Sum-Frequency Generation Vibrational Spectroscopy of Molecular Surfaces and Interfaces: Lineshape, Polarization, and Orientation. *Annu. Rev. Phys. Chem.* **2015**, *66* (1), 189–216. https://doi.org/10.1146/annurev-physchem-040214-121322.

(51) Moad, A. J.; Simpson, G. J. A Unified Treatment of Selection Rules and Symmetry Relations for Sum-Frequency and Second Harmonic Spectroscopies. *J. Phys. Chem. B* **2004**, *108* (11), 3548–3562. https://doi.org/10.1021/jp035362i.

(52) Niu, Y.; Zhao, J.; Zhang, X.; Wang, X.; Wu, J.; Li, Y.; Li, Y. Large Area Orientation Films Based on Graphene Oxide Self-Assembly and Low-Temperature Thermal Reduction. *Appl. Phys. Lett.* **2012**, *101* (18), 181903. https://doi.org/10.1063/1.4764549.

(53) Wagner, J. C.; Wu, Z.; Wang, H.; Xiong, W. Imaging Orientation of a Single Molecular Hierarchical Self-Assembled Sheet: The Combined Power of a Vibrational Sum Frequency Generation Microscopy and Neural Network. *J. Phys. Chem. B* **2022**, *126* (37), 7192–7201. https://doi.org/10.1021/acs.jpcb.2c05876.

(54) Wang, Z.; Fu, L.; Yan, E. C. Y. C–H Stretch for Probing Kinetics of Self-Assembly into Macromolecular Chiral Structures at Interfaces by Chiral Sum Frequency Generation Spectroscopy. *Langmuir* **2013**, *29* (12), 4077–4083. https://doi.org/10.1021/la304954h.

(55) Xiong, Q.; Jiang, Y.; Cai, X.; Yang, F.; Li, Z.; Han, W. Conformation Dependence of Diphenylalanine Self-Assembly Structures and Dynamics: Insights from

Hybrid-Resolution Simulations. *ACS Nano* **2019**, *13* (4), 4455–4468. https://doi.org/10.1021/acsnano.8b09741.

(56) Li, Q.; Jia, Y.; Dai, L.; Yang, Y.; Li, J. Controlled Rod Nanostructured Assembly of Diphenylalanine and Their Optical Waveguide Properties. *ACS Nano* **2015**, *9* (3), 2689–2695. https://doi.org/10.1021/acsnano.5b00623.

(57) Jackson, M.; Mantsch, H. H. The Use and Misuse of FTIR Spectroscopy in the Determination of Protein Structure. *Crit. Rev. Biochem. Mol. Biol.* **1995**, *30* (2), 95–120. https://doi.org/10.3109/10409239509085140.

(58) Seo, J.; Hoffmann, W.; Warnke, S.; Huang, X.; Gewinner, S.; Schöllkopf, W.; Bowers, M. T.; von Helden, G.; Pagel, K. An Infrared Spectroscopy Approach to Follow β-Sheet Formation in Peptide Amyloid Assemblies. *Nat. Chem.* **2017**, *9* (1), 39–44. https://doi.org/10.1038/nchem.2615.

(59) Barth, A. Infrared Spectroscopy of Proteins. *Biochim. Biophys. Acta - Bioenerg.* **2007**, *1767* (9), 1073–1101. https://doi.org/10.1016/j.bbabio.2007.06.004.